2006

Dual-polarized C- and Ku-band ocean backscatter response to hurricane-force winds

Stephen Frasier, *University of Massachusetts - Amherst*
D. Esteban-Fernandez
J. R Carswell
P. S Chang
P. G black, et al.

Dual-polarized C- and Ku-band ocean backscatter response to hurricane-force winds

D. Esteban Fernandez,[1,2] J. R. Carswell,[3] S. Frasier,[1] P. S. Chang,[4] P. G. Black,[5] and F. D. Marks[5]

Received 9 May 2005; revised 13 March 2006; accepted 15 April 2006; published 9 August 2006.

[1] Airborne ocean backscatter measurements at C- and Ku-band wavelengths and H and V polarizations at multiple incidence angles obtained in moderate to very high wind speed conditions (25–65 m s^{-1}) during missions through several tropical cyclones are presented. These measurements clearly show that the normalized radar cross sections (NRCS) response stops increasing at hurricane-force winds for both frequency bands and polarizations except for high incidence angles at C-band and H polarization. The results also show the mean NRCS departing from a power law behavior for all the presented frequency bands, polarizations, and incidence angles, suggesting a reduction in the drag coefficient. The overall flattening of the azimuthal response of the NRCS is also very apparent in all cases. A new set of geophysical model functions (GMFs) at C- and Ku-band are developed from these direct ocean backscatter observations for ocean surface winds ranging from 25 to 65 m s^{-1}. The developed GMFs provide a much more accurate characterization of the NRCS versus wind speed and direction, and their implementation in operational retrieval algorithms from satellite-based scatterometer observations would result in better wind fields. The differences between these measurements and other currently available GMFs, such as QuikSCAT, NSCAT2, CMOD4, and CMOD5, are reported. The implementation of these GMFs in retrieval algorithms will result in better wind fields from satellite-based scatterometers measurements.

Citation: Fernandez, D. E., J. R. Carswell, S. Frasier, P. S. Chang, P. G. Black, and F. D. Marks (2006), Dual-polarized C- and Ku-band ocean backscatter response to hurricane-force winds, *J. Geophys. Res.*, *111*, C08013, doi:10.1029/2005JC003048.

1. Introduction

[2] Tropical cyclones (TCs) pose more of a threat to the United States than ever before. Millions of people live and vacation along the coastline, and the construction of homes and businesses in coastal areas is on the increase. In many of these communities, evacuation routes are limited, requiring more time to prepare. Over the last 2 decades, our ability to predict the track of TCs has improved at approximately one percent a year [*McAdie and Lawrence*, 1993], while the population in areas that are most prone to landfalling TCs has increased at three to four percent a year [*Sheets*, 1990]. The accuracy and lead time of track and intensity forecasts for these storms must improve to significantly reduce the threat to lives and property.

[3] To improve the forecasts and analyses of the pattern, extent, track and intensity of TCs, a variety of research programs have focused on improving observations of several key parameters [*Marks and Shay*, 1998]. One of these parameters is the surface wind field. Airborne and spaceborne wind scatterometry may provide a means to measure the ocean surface wind field within TCs. *Katsaros et al.* [2000] demonstrated improved skill in detecting TC development using scatterometer winds from QuikSCAT. *Isaksen and Stoffelen* [2000] showed that ERS scatterometer winds had a positive impact on TC analyses and forecasts at the European Centre for Medium-Range Weather Forecasts (ECMWF). *Quilfen et al.* [1998] showed the potential of C-band scatterometry to aid in monitoring and forecasting of TCs, but pointed out that the winds were underestimated within the TC owing to CMOD4 [*Stoffelen and Anderson*, 1997] overestimating the normalized radar cross section (NRCS) of the ocean surface for high wind speeds. Others have also found the scatterometer winds to be anomalously low and have developed new ocean surface NRCS geophysical model functions (GMFs) for high wind speeds using satellite-based scatterometer NRCS measurements and surface wind fields predicted by TC models [*Jones et al.*, 1999; *Yueh et al.*, 2000]. *Yueh et al.* [2001] used QuikSCAT observations together with collocated SMM/I rain rate estimates to derive a modified NSCAT2 GMF and applied it to the particular case of Hurricane Floyd. Further work by *Yueh et al.* [2003] used Holland's model to improve wind retrievals for tropical cyclones from QuikSCAT observations at Ku-band. Though retrievals using these new

[1]University of Massachusetts, Amherst, Massachusetts, USA.
[2]Now at Office of Research and Applications, NOAA/NESDIS, Camp Springs, Maryland, USA.
[3]Remote Sensing Solutions, Barnstable, Massachusetts, USA.
[4]Office of Research and Applications, NOAA/NESDIS, Camp Springs, Maryland, USA.
[5]Hurricane Research Division, NOAA/AOML, Miami, Florida, USA.

0148-0227/06/2005JC003048

GMFs provide higher wind speeds, more work is needed to fully define the relationship between the NRCS and the ocean surface wind vector at high wind speeds to clarify the limitations of wind scatterometry.

[4] The first successful airborne scatterometer measurements in hurricane wind conditions were probably acquired through Hurricane Tina in 1992 by the University of Massachusetts' (UMass) C-band scatterometer [*Carswell et al.*, 1994]. A GMF valid up to moderate wind conditions was derived from the vertically polarized C-band measurements. Dual-polarized Ku-band airborne measurements up to 35 m s^{-1} were successfully acquired by the JPL NUSCAT scatterometer during a field campaign in 1997. From these observations, a new Ku-band GMF modified from the NSCAT-2 GMF was presented by *Yueh et al.* [2000]. Work by *Donnelly et al.* [1999] presented C- and Ku-band NRCS observations at V polarization for wind speeds as high as 45 m s^{-1} and 32 m s^{-1}, respectively. The authors showed that the C-band NRCS sensitivity to wind speed decreases for wind speeds greater than 20 m s^{-1}. The CMOD4 GMF does not account for this change in sensitivity, and therefore it overpredicts the NRCS at high winds. As a result, the ERS Active Microwave Instrument (AMI) derived winds that use this GMF are too low for high wind speeds. *Donnelly et al.* [1999] developed a new model, CMOD4HW, which incorporates this reduction in sensitivity, and these results were used in the derivation of the currently operational CMOD5 GMF [*Hersbach*, 2003]. The Ku-band NRCS measurements presented by *Donnelly et al.* [1999] also showed sensitivity differences compared with NSCAT1 [*Wentz and Smith*, 1999], but the data set was limited to 32 m s^{-1} so that the results could not be extended to hurricane-force winds (>35 m s^{-1}).

[5] New GMFs were presented by *Carswell et al.* [2000] at C- and Ku-band and V polarization for wind speeds ranging from 15 to 55 m s^{-1}. These GMFs were derived from measurements acquired with the University of Massachusetts (UMass) C- and Ku-band scatterometers, hereafter CSCAT and KUSCAT, during flights through Hurricanes Brett, Dennis, and Floyd. These measurements indicated a decreased sensitivity at both frequency bands above 45 m s^{-1}.

[6] UMass participated in several research/reconnaissance flights in 2002 and 2003 through Hurricanes Lili (2002), Fabian, and Isabel (2003). For the first time, dual-polarized C- and Ku-band (roughly 5.3 and 13.5 GHz, respectively) ocean surface NRCS measurements were simultaneously collected with the UMass Imaging Wind and Rain Airborne Profiler (IWRAP), a high-resolution dual-band dual-polarized conically scanning airborne Doppler radar. This radar was designed to study the ocean surface backscatter at low to extreme wind conditions, to analyze the impact of rain on the backscatter measurements, and to study the inner core of TCs [*Fernandez et al.*, 2005]. In this paper we present coincident vertical and horizontal polarized, high-resolution C- and Ku-band NRCS observations of ocean surface wind speed events from 25 to 65 m s^{-1} in absolutely precipitation free areas and at several incidence angles. Contrary to other airborne systems, IWRAP directly profiles the Doppler and reflectivity from precipitation volume backscatter. This ensures that the precipitation and ocean backscatter observations are coincident and simultaneous, which is critical since precipitation varies significantly both spatially and temporally and even small amount of precipitation will bias the results, particularly at Ku-band.

Table 1. Hurricane Flight Summaries

Date	Hurricane	Saffir-Simpson Scale (Maximum Wind Speed)
30 September 2002	Lili	Cat. 2 (45 m s^{-1})
2 October 2002	Lili	Cat. 4 (67 m s^{-1})
2 September 2003	Fabian	Cat. 3 (50 m s^{-1})
3 September 2003	Fabian	Cat. 4 (55 m s^{-1})
4 September 2003	Fabian	Cat. 3 (57 m s^{-1})
12 September 2003	Isabel	Cat. 5 (72 m s^{-1})
13 September 2003	Isabel	Cat. 5 (67 m s^{-1})
14 September 2003	Isabel	Cat. 5 (61 m s^{-1})
16 September 2003	Isabel	Cat. 4 (41 m s^{-1})
18 September 2003	Isabel	Cat. 2 (64 m s^{-1})

[7] From all these measurements, a new set of GMFs that cover the complete range of angles used by satellite ocean wind scatterometry has been developed. These results show that the ocean NRCS at Ku-band wavelengths saturates and begins to decrease with wind speed at both polarizations and all incidence angles. The C-band vertically polarized GMFs show the same saturation effect. The C-band horizontally polarized GMF, which constitutes the first model available at this frequency band and polarization, reveals instead a virtually nonsaturating behavior at high incidence angles and for wind speeds as high as 65 m s^{-1}.

[8] The paper is organized as follows: The experiments, instruments, and processing methods are described in section 2. Section 3 presents the NRCS measurements and reports differences between them and current GMFs CMOD5, NSCAT2 and QuikSCAT. New C- and Ku-band GMFs are developed for high wind speeds in section 4. The impact that these results have on satellite-based wind scatterometry for observing TCs and severe ocean storms is addressed in the conclusions.

2. Instrumentation and Processing Methods

[9] During the 2002 and 2003 hurricane seasons, IWRAP and the UMass Simultaneous multi-Frequency Microwave Radiometer (SFMR) were installed on the NOAA WP-3D aircraft for the Office of Naval Research (ONR) CBLAST Program and the National Oceanic and Atmospheric Administration (NOAA/NESDIS) Hurricane Ocean Winds and Rain Experiment. A total of 10 missions were flown through Hurricanes Lili (2002), Fabian and Isabel (2003). Eight of the 10 missions were over open ocean and included several passes directly through the hurricane eye during various phases of these systems (Table 1 summarizes these flights). Wind speeds as high as 74 m s^{-1} were sampled, with wind speeds reaching 65 m s^{-1} in rain-free conditions. Summaries of these flights can be found at the HRD web site (http://www.aoml.noaa.gov/hrd/cblast/index.html).

2.1. SFMR

[10] The SFMR is a C-band nadir viewing radiometer that measures the emission from the ocean surface and atmosphere simultaneously at six separate frequencies: 4.63, 5.5, 5.915, 6.344, 6.6 and 7.05 GHz [*Knapp et al.*, 2000]. The

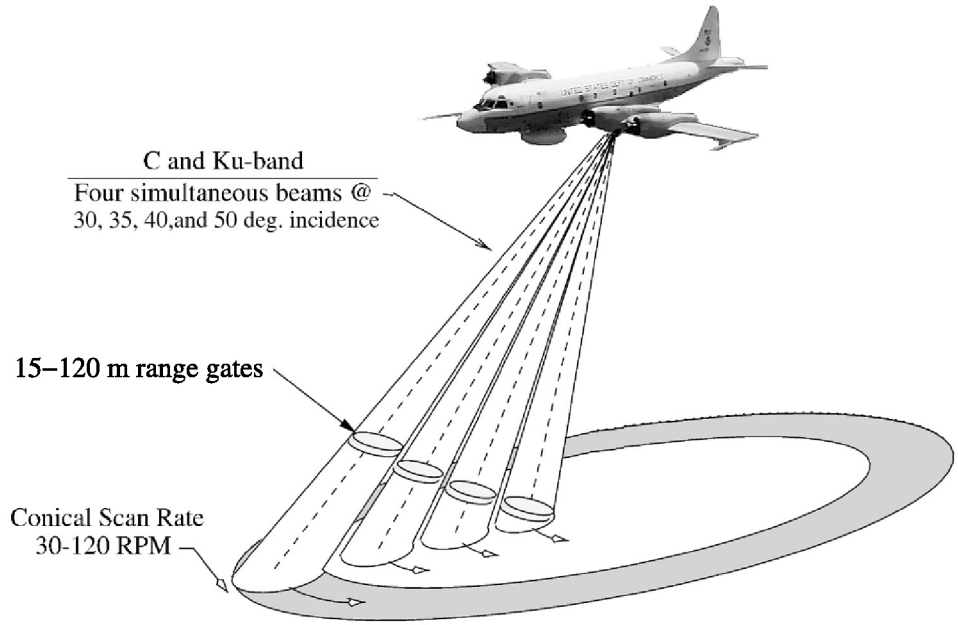

Figure 1. Measurement geometry for the IWRAP instrument.

SFMR measurement precision (ΔT) is approximately 0.4 K for a 50-ms integration time. Since the 1980s, this type of instrument has been used during hurricane season to remotely sense the surface wind speed and the column rain rate within the instrument's field of view [*Jones et al.*, 1981]. The winds reported by these instruments are equivalent to a 10-m 10-min averaged neutral stability wind speed (U_{10N}) [*Uhlhorn and Black*, 2003]. In 1999, the HRD Stepped Frequency Microwave Radiometer became an operational instrument providing real-time wind speed and rain-rate measurements that were telemetered via the GOES Aircraft Satellite Data-Link (ASDL) to the National Hurricane Center (NHC) during the hurricane research flights. Note that the only difference between the HRD SFMR and the UMass SFMR is that the UMass system acquires its measurements from all six channels simultaneously rather than time multiplexing through the frequencies. For the 2000 hurricane season, NHC declared the SFMR a national need. On the basis of its performance in 1999, the UMass SFMR, which also reports real-time wind speeds and rain rates, was incorporated operationally into the ASDL system.

[11] The SFMR brightness temperature (T_B) measurements are sampled at 20 Hz and averaged to 1 Hz, resulting in a $\Delta T < 0.1$ *K*. At the nominal aircraft speed of 125 m s^{-1}, this results in a spatial resolution of roughly 1 km. For a given sea surface temperature (SST), the change in emissivity is directly related to T_B. The dependence of microwave attenuation from rainfall with frequency provides a means of retrieving the quantity of liquid precipitation in the atmospheric column below the aircraft as well. The six simultaneous measurements at different frequencies of the scene provide an overdeterminated system which is used to infer the best wind speed and rain rate estimates in the least mean square sense. The U_{10N} and rain rates (R_r) are derived from the 1-Hz averaged T_B measurements. The accuracy of the SFMR U_{10N} estimates is better than ±1.5 m s^{-1} for wind speeds as high as 70 m s^{-1} [*Jones et al.*, 1981]. All U_{10N} estimates used to develop the GMFs from IWRAP NRCS measurements in this paper are derived from SFMR.

2.2. IWRAP

[12] IWRAP is a conically scanning dual-polarized (H and V polarizations) dual-frequency (C- and Ku-band) airborne Doppler radar that measures Doppler velocity and reflectivity profiles from precipitation as well as ocean surface backscatter at 15- to 150-m resolution simultaneously at four different incidence angles (approximately 30, 35, 40 and 50 degrees) [*Fernandez et al.*, 2005]. Figure 1 illustrates the measurement technique employed by this instrument. At a nominal conical scanning rate of 60 RPM, IWRAP measures the full azimuthal backscatter response at four incidence angles, two frequencies and two polarizations every second. Both instruments employ internal calibration loops to measure and correct fluctuations in the transmitter and receiver gain to within 0.1 dB.

[13] IWRAP's digital acquisition system incorporates a pulse-pair processor, implemented as a magnitude and covariance estimate of the demodulated echo for each range gate (the covariance estimate uses the range gate from the previous profile), and the result is summed on a per-range gate basis. Among other functions, the pulse-pair processor provides the averaged magnitude ($\hat{S}_{xx}$), expressed as

$$\hat{S}_{xx} = \frac{1}{M}\sum_{m=0}^{M-1} |V_{xxm}|^2, \tag{1}$$

where $V_{xxm} = I_{xxm} + Q_{xxm}$ is the complex signal with the *xx* subscript denoting the transmit and receive polarization, and *M* giving the number of profiles to average. The pulse-pair

processor also provides the real (DI_{xx}) and imaginary (DQ_{xx}) parts of the complex covariance estimate (i.e., the autocorrelation function, $\hat{R}_{xx}$). At a given range gate r_g, $\hat{R}_{xx}$ is given by [see *Doviak and Zrnic*, 1984]

$$\hat{R}_{xx}(r_g) = DI_{xx}(r_g) + jDQ_{xx}(r_g) = \frac{1}{M}\sum_{m=0}^{M-1} V_{xx_m}^{*}(r_g)\, V_{xx_{m+1}}(r_g), \quad (2)$$

where * denotes complex conjugate.

[14] The NRCS can thus be derived from the IWRAP measurements of the magnitude by applying the radar range equation,

$$\sigma^o = \frac{(4\pi)^3 K_c \hat{S}_{xx}}{P_t \lambda^2 \int_{A_{ill}} (G^2/R^4)\, dA}, \quad (3)$$

where σ^o is the NRCS, K_c is a calibration constant that converts the magnitude estimate $\hat{S}_{xx}$ to actual absolute receive power, A_{ill} is the area illuminated by the antenna footprint, P_t is the transmit power, G is the antenna gain, λ is the radar wavelength and R is the distance to the surface. The NRCS values are then separated by frequency band, polarization and incidence angle. For each one, the following processing is performed.

[15] The NRCS measurements from each conical scan are separated by incidence angle and then averaged into thirty-two 11.25 degree azimuth bins. A total of 62 consecutive samples (i.e., M = 62 in equations (1) and (2)) are used by the pulse-pair processor to derive the amplitude and covariance estimates for each bin. The averaged measurements are then corrected for gain drifts, and the receiver noise power is subtracted. The aircraft attitude data are used to reference each azimuthal bin to true north and to calculate the instantaneous incidence angle for computation of the NRCS. Pitch and roll motions of the aircraft cause the instantaneous incidence angle to vary around the nominal pointing angles; the NRCS measurements are thus also binned by instantaneous incidence angle in one-degree steps.

[16] To evaluate the NRCS azimuth modulation dependence on the ocean surface wind speed, the following procedures are performed. First, the ocean surface wind direction is determined using the scatterometer data and using flight-level wind direction and SFMR wind speed estimates. For this purpose, all the NRCS azimuth bins are mapped onto 0.5-km along-track cells based upon GPS latitude and longitude data and the measurement geometry. For each azimuth bin, all pixels acquired within each 0.5-km along-track cell acquired at the same incidence angle are averaged together. This results in 32 azimuth bins per incidence angle containing 0.5-km averaged NRCS values. Figure 2 illustrates this binning scheme. The three-term Fourier series given below is fit to the 0.5-km NRCS along-track cell values,

$$\sigma^\circ(\theta,\chi) = A_0(\theta) + A_1(\theta)\cos(\chi) + B_1(\theta)\sin(\chi) + A_2(\theta)\cos(2\chi) + B_2(\theta)\sin(2\chi), \quad (4)$$

where θ is the incidence angle and χ is the azimuth look direction relative to true North. In most cases, there are two maxima in the NRCS, one in the upwind direction and one in the downwind direction. At moderate incidence angles (roughly 30 to 55 degrees), there is a well-known asymmetry between these upwind and downwind maxima [*Plant*, 1986], with a higher maximum in the upwind direction, which is consistent with the predictions of the combined tilt and hydrodynamic modulation of the Bragg-resonant small-scale waves by the large-scale waves. This asymmetry persists even in high wind regimes, as will be discussed in section 3. For the IWRAP measurements, the azimuth locations of the these maxima are determined from this fit. To select which maxima represents the upwind direction, a rough estimate of the ocean surface wind direction is first determined from the flight level wind direction, which is measured by onboard sensors at typical flying altitudes of 1.5 to 2 km. The maxima closest to the estimated surface wind direction is chosen as the upwind direction (χ_{up}). Note that meteorological definition for upwind direction is used. This approach will maintain the phase of the first harmonic (A_1 in equation (4)) in case this term becomes negative at the high wind speeds (i.e., maximum in the downwind rather than upwind direction). The SFMR wind speed estimates are used to identify and correct cases where the hurricane eye at flight altitude is offset from the eye at the surface. In these cases, where there could be a large discrepancy between the flight level and the surface level wind directions, the IWRAP measurements are not used in the development of empirical GMFs.

[17] The 0.5-km NRCS along-track values are only used to determine the surface wind direction. Given χ_{up}, the original single-scan NRCS measurements are further binned by SFMR U_{10N} estimates. During hurricane eye-wall penetrations, where wind gradients can be large, the SFMR U_{10N} estimates closest in distance rather than in time were

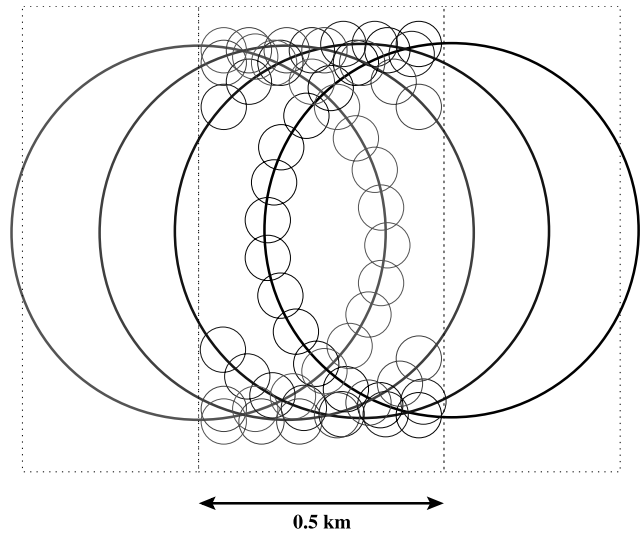

Figure 2. Simplified scheme of the binning procedure. The conical scan is divided into 32 bins, and for each incidence angle, all the looks from all conical scans acquired within a given 0.5-km along-track cell that fall in each azimuth bin are averaged together.

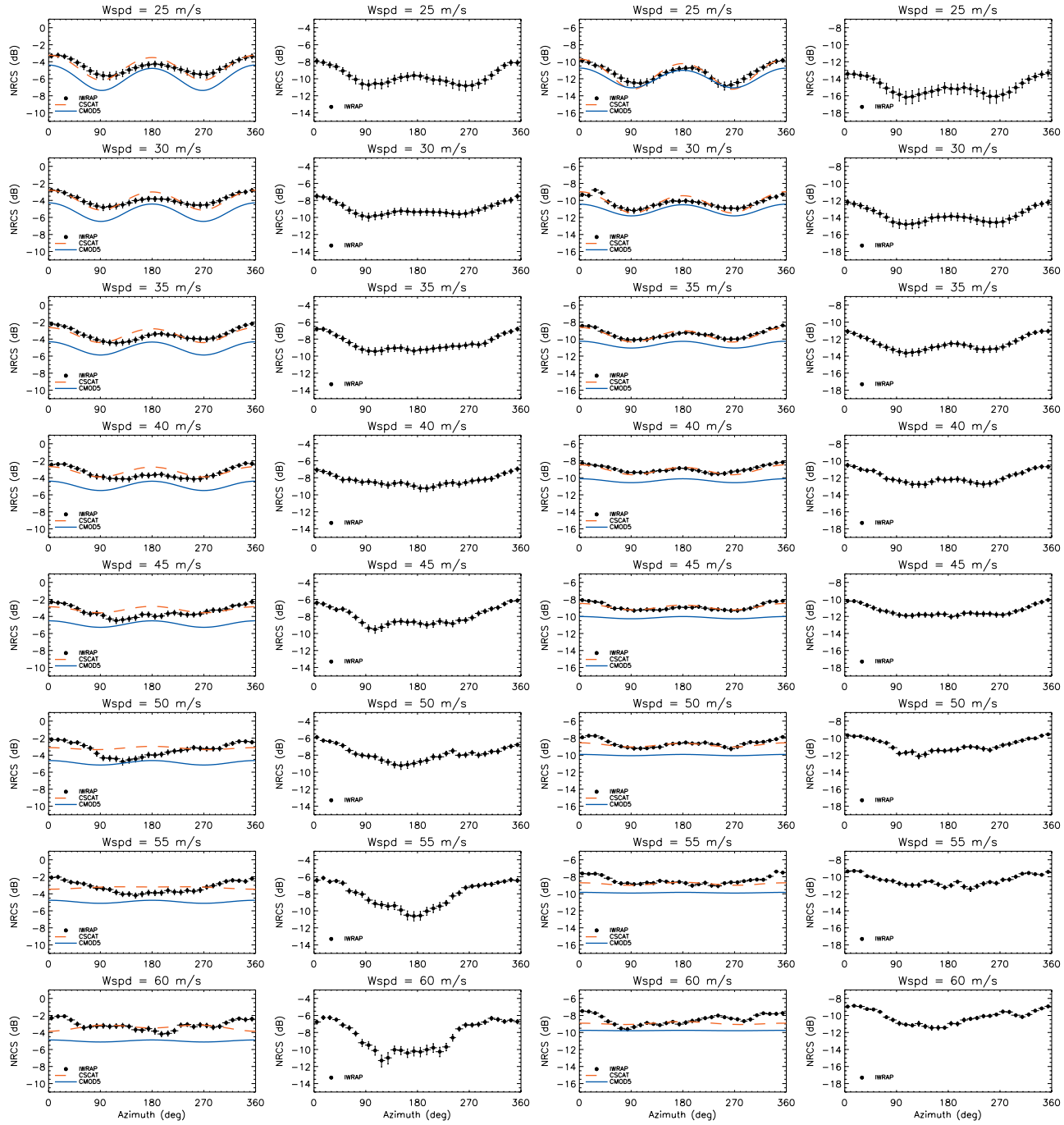

(a) C−band V 29 deg. (b) C−band H 31 deg. (c) C−band V 50 deg. (d) C−band H 49 deg.

Figure 3. Measured C-band NRCS measurements at two of the incidence angles (30 and 50 degrees approximately) for both V and H (solid circles) plotted versus azimuth at U_{10N} ranging from 25 to 60 m s^{-1} in 5 m s^{-1} steps. The vertical and horizontal bars represent the standard deviation of the NRCS measurements and of the azimuth positions for each azimuth bin, respectively. The CMOD-5 (solid blue line) and CSCAT (dashed red line) GMFs are overlaid at V polarization. There is currently no other GMF available at H polarization.

used. At any given instant and for each azimuth bin, the corresponding along-track distance (ahead or behind the aircraft position) was calculated, and the SFMR U_{10N} for the projected position was used in the binning.

[18] In this way, and for each frequency band, polarization and incidence angle, a final NRCS table is obtained for every conical scan with the following dimensions: σ° (θ, U_{10N}, χ). This allows us to retrieve

the full azimuthal response of the ocean backscatter at all wind speeds. The real coefficients of the three-term Fourier cosine series,

$$\sigma^{\circ}(\theta, U_{10N}, \chi) = A_0 + A_1 \cdot \cos(\chi_{up} - \chi) + A_2 \cdot \cos(2[\chi_{up} - \chi]), \quad (5)$$

can be calculated from the expressions

$$A_0 = \frac{1}{N}\sum_{n=1}^{N}\sigma^{\circ}(\chi_n) \quad (6)$$

$$A_{i=\{1,2\}} = \frac{2}{N}\sum_{n=1}^{N}[\sigma^{\circ}(\chi_n)\cdot\cos(i\chi_n)], \quad (7)$$

where N is the number of azimuth bins. A_0, A_1, and A_2 are functions of θ and U_{10N}.

2.3. Rain Flagging

[19] The presence of precipitation can contaminate the backscatter measurements in three different ways: (1) the microwave signal is attenuated by the rain drops resulting in an underestimate of the NRCS; (2) part of the radar signal is scattered by the rain drops resulting in an overestimate of the NRCS due to volume backscatter; and (3) the ocean surface roughness is perturbed by the impinging rain drops, thereby influencing the surface backscatter measurements. These effects must be either removed before evaluating the sensitivity of the mean NRCS (A_0) measurements on U_{10N}, or the rain contaminated samples need to not be considered in the analysis. Since IWRAP provides reflectivity and Doppler profiles of precipitation volume backscatter, the presence of rain can easily be checked together with every ocean NRCS measurement. The filtering is implemented by means of a threshold on the range-gate averaged normalized spectral width $\bar{\hat{\sigma}}_{vn}$ (i.e., the second moment of the Doppler Spectrum),

$$\bar{\hat{\sigma}}_{vn_{xx}} = \frac{1}{\pi\sqrt{2}r_g}\sum_{i=1}^{r_g}\left|\ln\left(\frac{\hat{P}_{xx}(i)}{|\hat{R}_{xx}(i)|}\right)\right|^{1/2}, \quad (8)$$

where r_g is the total number of range gates in the profile before reaching the ocean surface and $\hat{P}_{xx}(i)$ is the signal power estimate after noise removal at range gate i. When rain is not present, the ratio inside the logarithm approaches unity, and therefore the normalized spectral width tends to very small values. The presence of rain results in smaller values of the autocorrelation function, and therefore to larger values of the spectral width. The spectral widening increases with an increasing rainfall rate. Therefore this parameter is well suited for the detection of rain in a profile, and shows a better sensitivity than the magnitude measurements alone. The variance in the spectral width estimator is further improved by averaging the single range gate estimates for the entire profile before reaching the ocean surface, thus resulting in an increased sensitivity to rain. For the analysis in this paper, all rain flagged ocean NRCS measurements have been excluded.

3. Ocean Surface NRCS Observations of Tropical Cyclones

3.1. NRCS

[20] The C- and Ku-band NRCS measurements are rain flagged and averaged into 3 m s^{-1} wind speed bins based on U_{10N} measurements. Figure 3 shows the averaged C- and Ku-band NRCS measurements versus azimuth for both V and H polarizations at wind speed ranging from 25 to 65 m s^{-1} in steps of 5 m s^{-1}. The CMOD5, CSCAT, KUSCAT, NSCAT2 and QuikSCAT GMFs are overlaid. A discussion of the mean NRCS levels among the GMFs shown in these figures will be left for the next section, where conclusions will be drawn on the basis of the A_0 measurements. In this section we will only discuss the general behavior (i.e., the modulation) of the GMFs versus azimuth at different wind speeds.

[21] These figures show primarily two different and important features: (1) There is a significant flattening of the central part of the azimuthal response (roughly from 90 to 270 degrees from upwind direction) for most frequencies and polarizations at high wind speeds. This implies the loss of the different backscatter response (or signature) in the downwind and crosswind directions. This characteristic is not captured by any of the GMFs used in this analysis, and it cannot be easily represented by the first two harmonics of the NRCS since there remains a very clear upwind versus downwind and crosswind signature (while the downwind versus crosswind ratio approaches unity, the upwind versus crosswind is still large); and (2) in most cases the downwind signature reappears after the azimuthal response has flattened. This will be discussed further with the A_0 results, where we will support the concept of a decoupling between the wind and the ocean surface (i.e., suggesting a reduction in the drag coefficient).

[22] A more detailed inspection of these figures also reveals other important features. At C-Band and V polarization, as shown in Figure 3, there is a good agreement between the IWRAP measurements and the CSCAT GMF for the lower wind speeds. The CMOD5 GMF overestimates the azimuthal modulation at the lowest incidence angle as well as for the lower wind speeds, but in all other cases the modulation greatly resembles the CSCAT behavior. Above 50 m s^{-1}, both the CSCAT GMF and the CMOD5 stop behaving properly and become virtually flat for all azimuth directions. As anticipated, our measurements start showing the flattening of the downwind signature above approximately 45 m s^{-1}, and also after that the upwind/downwind difference increases in most cases. The H polarized measurements present an ever earlier loss of the downwind signature, and a highly increased upwind/downwind ratio after that. At Ku-band and V polarization, as shown in Figure 4, the NSCAT2 GMF overpredicts the azimuthal modulation in most cases, and above 35 m s^{-1} the difference is very large in all cases. There is an excellent agreement with the KUSCAT GMF up to 45 m s^{-1}, and the QuikSCAT GMF (shown at a different incidence angle since this model function is only available for 51

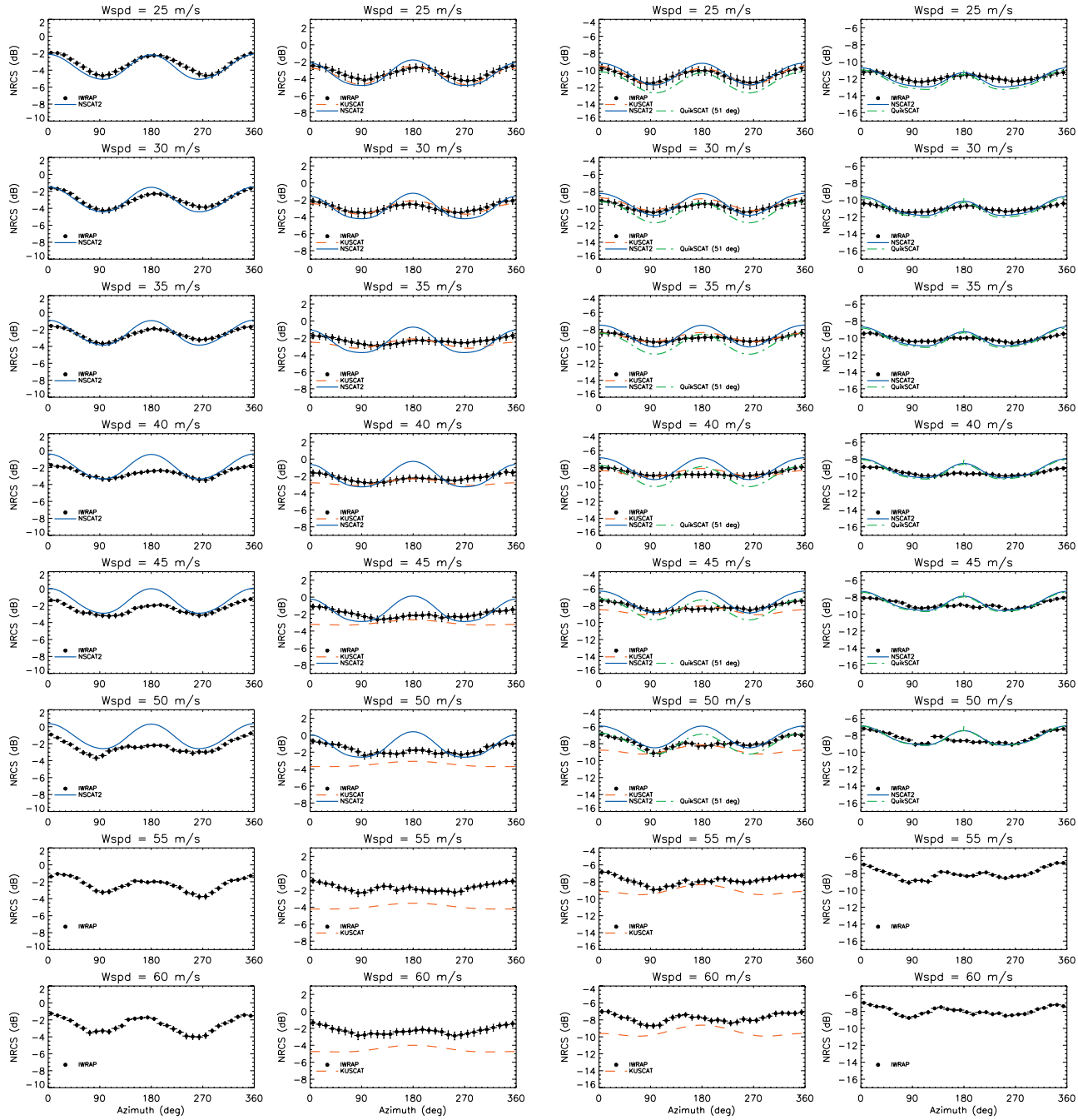

(a) Ku-band V 29 deg. (b) Ku-band H 29 deg. (c) Ku-band V 48 deg. (d) Ku-band H 48 deg.

Figure 4. Measured Ku-band NRCS measurements at two of the incidence angles (30 and 50 degrees approximately) for both V and H (solid circles) plotted versus azimuth at U_{10N} ranging from 25 to 60 m s^{-1} in 5 m s^{-1} steps. The vertical and horizontal bars represent the standard deviation of the NRCS measurements and of the azimuth positions for each azimuth bin, respectively. The NSCAT2 (solid blue line), KUSCAT (red dashed line), and QuikSCAT (dash-dotted green line) GMFs are overlaid. Note that at V polarization, the QuikSCAT GMF is only available from 51 to 60 degrees incidence, and so it is shown at 51 degrees incidence. This introduces a bias associated to the different incidence angle but shows nevertheless the nonsaturating trend with an increasing wind speed.

to 60 degrees incidence at this polarization) seems to overpredict the modulation as well and fails to estimate the downwind flattening. Our measurements show that the downwind signature reappears above 55 m s^{-1}. At H polarization, the NSCAT2 GMF manifests a good agreement with the IWRAP measurements only at the lowest wind speeds, and it does not decrease its modulation after that. The QuikSCAT GMF follows the same behavior,

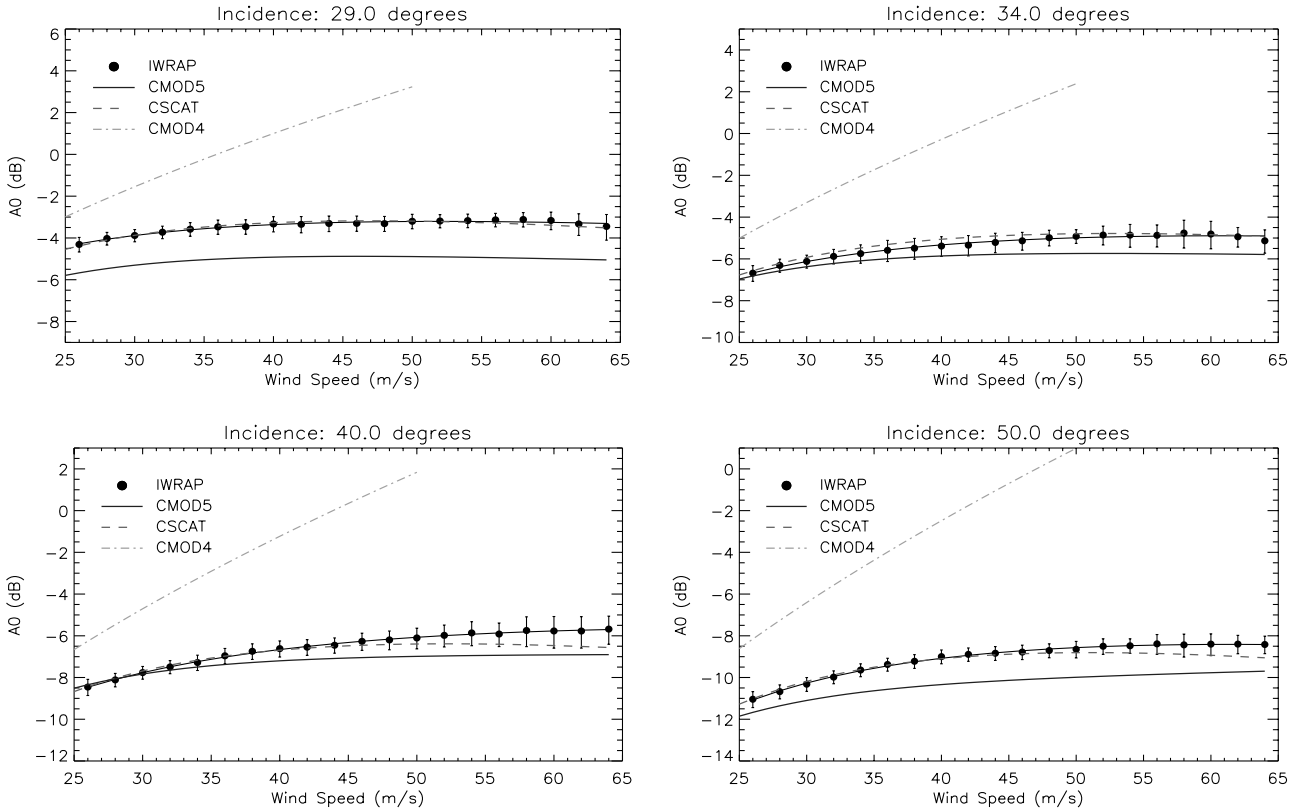

Figure 5. Averaged IWRAP A_0 measurements at C-band and V polarization (solid circles) plotted versus the mean U_{10N} estimates. Standard deviations of the A_0 measurements within each 2 m s^{-1} wind speed bin are shown by the vertical lines. From these measurements, the derived high wind speed IWRAP GMF (discussed in section 4) is also plotted (solid black line). The CMOD-5 (dash-dotted line) and CSCAT (dashed line) GMFs are overlaid.

and fails to flatten the downwind signature above 40 m s^{-1}. Again, the downwind response enhances above 50 m s^{-1}.

3.2. Mean NRCS (A_0)

[23] The C- and Ku-band A_0 measurements are rain flagged and averaged into 2 m s^{-1} wind speed bins on the basis of the U_{10N} measurements. For each bin, the mean U_{10N} value is also calculated. Figures 5 through 8 plot the averaged C- and Ku-band A_0 measurements versus the mean U_{10N} measurements. The CMOD4, CMOD5, CSCAT, KUSCAT, NSCAT2 and QuikSCAT GMFs are overlaid. The high wind speed model that will be developed in section 4 is plotted as solid lines.

[24] The figures show that the NSCAT2 GMFs significantly overestimates the A_0 measurements for wind speeds exceeding 45 m s^{-1}, and the CMOD4 GMF significantly overpredicts the A_0 measurements for wind speeds exceeding 25 m s^{-1}. Furthermore, these figures clearly show that the C- and Ku-band A_0 measurements saturate. That is, the A_0 measurements stop increasing with U_{10N}. In fact, the C-band A_0 measurements acquired at 29.0 and 34.0 degrees incidence (Figures 5 and 6) and the Ku-band V-polarized A_0 measurements acquired at all four incidence angles (Figure 7) actually start decreasing with higher wind speeds.

[25] The saturation effect and decrease in A_0 is predicted by the composite surface model (DP87) presented by *Donelan and Pierson* [1987]. The wave number spectrum used in the DP87 model saturates at high wind speeds for Bragg resonant wavelengths. The DP87 model predicts that this saturation occurs first at the smaller wavelengths, occurring at approximately 35 m s^{-1} for Ku-band and 45 m s^{-1} for C-band. This trend is consistent with the A_0 measurements presented in this paper, although at higher wind speeds (around 45 m s^{-1} for Ku-band and 55 m s^{-1} at C-band and V polarization). The only difference is that the DP87 model predicts the saturation wind speed decreases as the incidence angle increases. This is in contrast to our measurements (but in agreement with the observations used in the derivation of the CSCAT GMF). However, it is the specular backscatter contribution within the DP87 model that causes the lower incidence angles not to saturate as quickly and may be incorrectly modeled. The Bragg backscatter contribution in the DP87 model actually predicts the saturation to occur first at the lower incidence angles similar to this data set. The H polarized measurements present a higher-saturation wind speed, and a decrease in the A_0 is only present at the lowest incidence angle.

[26] The observed saturation effect is also in accordance with the results presented by *Powell et al.* [2003], where the authors show that the momentum transfer between atmosphere and ocean stops increasing with sea surface roughness and wind speed as the latter increases above hurricane force. The authors used more than 300 GPS dropwindsonde measurements launched from reconnaissance or re-

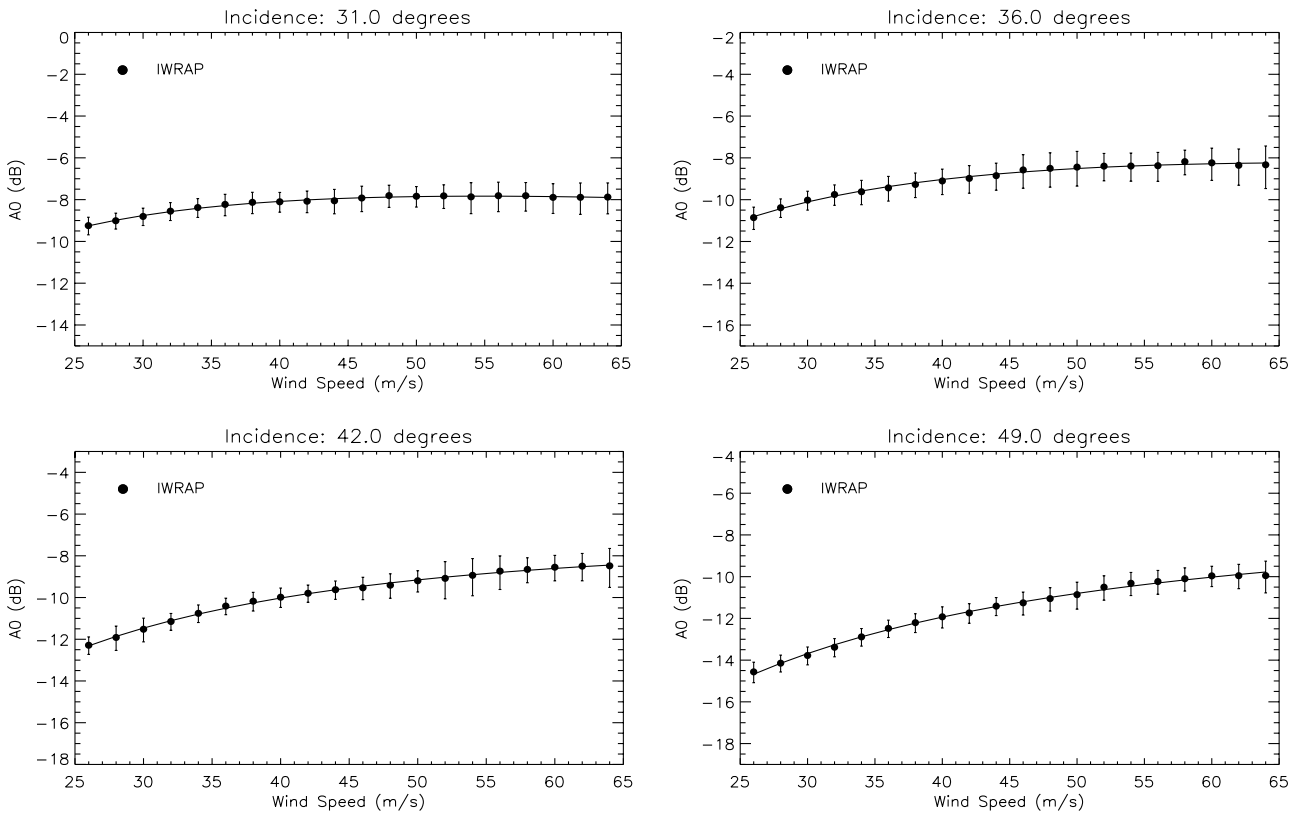

Figure 6. Averaged IWRAP A_0 measurements at C-band and H polarization (solid circles) plotted versus the mean U_{10N} estimates. Standard deviations of the A_0 measurements within each 2 m s^{-1} wind speed bin are shown by the vertical lines. From these measurements, the derived high wind speed IWRAP GMF (discussed in section 4) is also plotted (solid black line). There is currently no other GMF for this frequency band and polarization.

search aircrafts during missions through tropical cyclones over the span of 3 years. Work by *Donelan et al.* [2004] uses water tank observations to show that the drag coefficient stops increasing linearly in high winds, and offers an explanation based on separation of the air flow from the crests of steep storm waves. Our set of direct measurements of ocean backscatter constitutes, to our knowledge, the first direct observations in support of the saturation effect at both frequency bands and polarizations.

3.3. Normalized First Harmonic (a_1)

[27] The C- and Ku-band A_1 measurements are normalized by the mean NRCS ($a_1 = A_1/A_0$) and averaged into 2 m s^{-1} wind speed bins on the basis of the coincident U_{10N} measurements. Figure 9 plots the averaged a_1 measurements versus the mean U_{10N} measurements. The CMOD4, CMOD5, CSCAT, KUSCAT, NSCAT2 and QuikSCAT GMFs are overlaid. The high wind speed model that will be developed in section 4 is plotted as solid lines.

[28] As Figure 9 shows, the C-band a_1 measurements seem to slightly increase with increasing wind speed. The CMOD4 GMF predicts a similar trend, and while it is in very good agreement at 29.0 degrees incidence, it presents a large positive bias after that. Both the CMOD5 and the CSCAT GMFs present a decreasing trend with increasing wind speed. At Ku-band (Figure 10), the NSCAT2 GMF predicts a constant value for a_1, but is close in magnitude to the measurements at V polarization, while at H polarization the agreement is excellent. In general, the C- and Ku-band a_1 measurements approach zero at around 40 to 45 m s^{-1} wind speed, in agreement with the concept of a saturation. However, while the saturation in the A_0 measurements indicates a saturation in the wind speed, the fact that the a_1 values approach zero supports rather the concept of a saturation in the wind direction. In other words, the upwind and downwind directions become almost impossible to discriminate from these values.

[29] It is worth noting that especially at Ku-band the first harmonic seems to increase again after having approached zero, reaching a high peak at around 50 to 55 m s^{-1} wind speed. This is followed by a new decay, only to start increasing again. This is in agreement with the reappearance of the downwind signature with respect to the upwind direction discussed in the previous section. This kind of behavior has been observed as well in the measurements used to derive the CSCAT and KUSCAT GMFs. The parabolic fitting that will be used in section 4 to derive a model from the a_1 measurements will overlook this feature, as happened with the CSCAT and KUSCAT GMFs.

3.4. Normalized Second Harmonic (a_2)

[30] The C- and Ku-band A_2 measurements are normalized by the mean NRCS ($a_2 = A_2/A_0$) and averaged into 2 m s^{-1} wind speed bins on the basis of the coincident U_{10N}

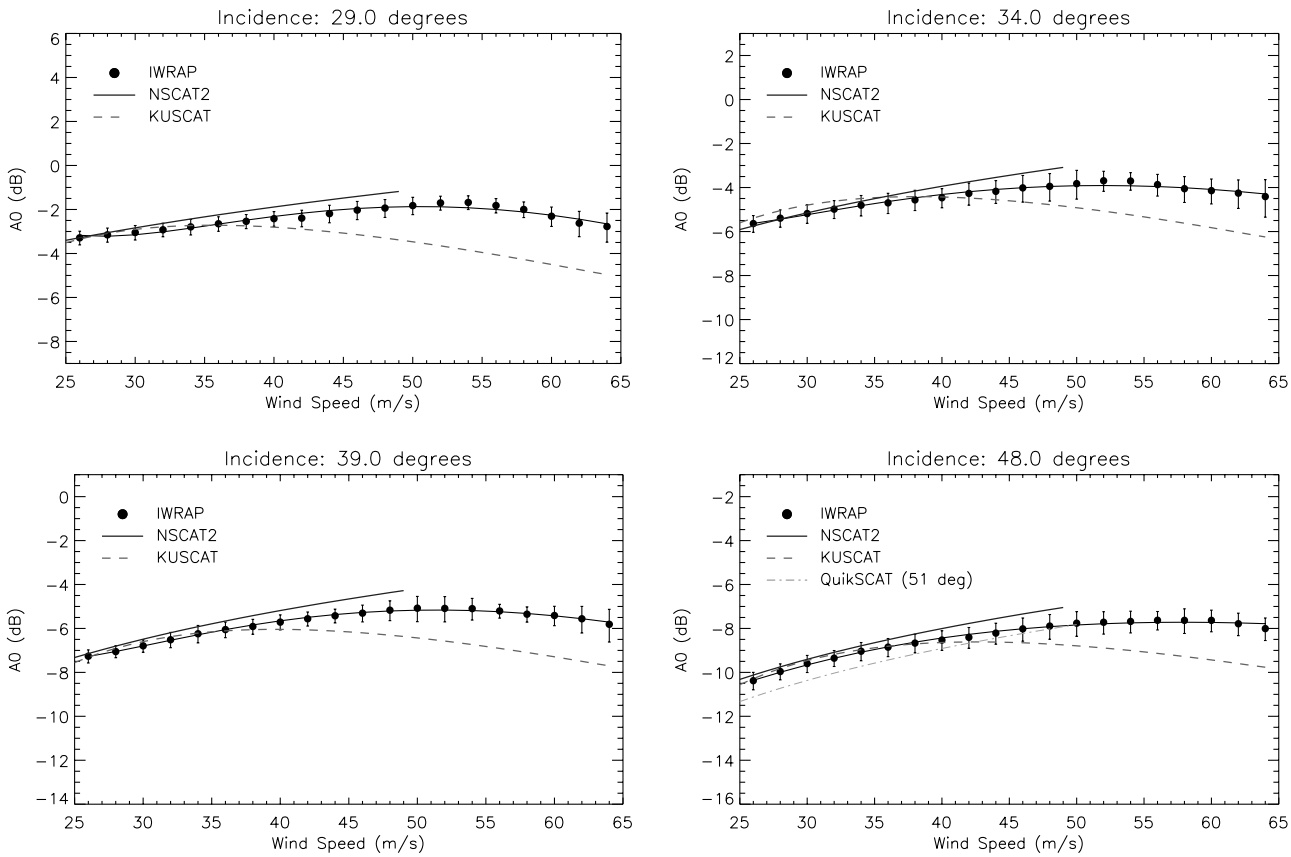

Figure 7. Averaged IWRAP A_0 measurements at Ku-band and V polarization (solid circles) plotted versus the mean U_{10N} estimates. The error bars show the standard deviations of the A_0 measurements within each 2 m s^{-1} wind speed bin. From these measurements, the derived high wind speed IWRAP GMF (discussed in section 4) is also plotted (solid black line). The NSCAT2 (dashed line) and KUSCAT (solid line) GMFs are overlaid.

measurements. Figure 11 plots the averaged a_2 measurements versus the mean U_{10N} measurements. The CMOD4, CMOD5, CSCAT, KUSCAT, NSCAT2 and QuikSCAT GMFs are overlaid. The high wind speed model that will be developed in section 4 is plotted as solid lines.

[31] The C- and Ku-band a_2 measurements decrease to very small values (<0.1) for wind speeds above 45 m s^{-1}, further supporting the concept of a full saturation: Together with a saturation in the wind speed and the upwind/downwind directions, as discussed before from the results on the mean NRCS and the first harmonic, the second harmonic suggests that the crosswind signature in the wind direction becomes almost negligible as well. In other words, the crosswind NRCS is approaching the upwind NRCS values as the wind speed approaches the saturation wind speed.

[32] However, as Figure 12 shows, at Ku-band the a_2 measurements start to increase again above 55 m s^{-1}. The same behavior is present in the a_1 measurements, where a peak at around 50 to 55 m s^{-1} appears in the a_2 measurements as well. This is also consistent with the reappearance of the downwind signature with respect to the crosswind direction. Again in this case, the parabolic fitting will remove this feature. All the GMFs also predict a decreasing a_2 with increasing wind speed, with the exception of the NSCAT2 GMF, where the values are too high and constant for all wind speeds shown. The CMOD4 GMF in Figure 11 follows the decreasing trend but shows large values in comparison to the rest of GMFs. None of the available GMFs predicts an increase of the a_2 values above 50 m s^{-1}.

4. High Wind Speed GMF

[33] C- and Ku-band high wind speed GMFs are developed by adding additional terms to a conventional power law. These terms permit a slow roll-off in the power law wind exponent and allows the saturation wind speed ($U_{10N_{sat}}$) to be determined. $U_{10N_{sat}}$ is defined as the wind speed where A_0 reaches its maximum value, i.e.,

$$\left.\frac{\partial A_0}{\partial U_{10N}}\right|_{U_{10N}=U_{10N_{sat}}} = 0. \tag{9}$$

Note that this value does not necessarily reflect the wind speed at which the measurements start to deviate from a power law behavior (the maximum in the A_0 will happen at a higher U_{10N}), but rather suggests the wind speed after which the A_0 response will start decreasing. In fact, at C-band and V polarization the A_0 response is virtually flat (within a few tenths of a dB) for more than 15 m s^{-1} above 40 m s^{-1}, and the meaning of the defined $U_{10N_{sat}}$ is less

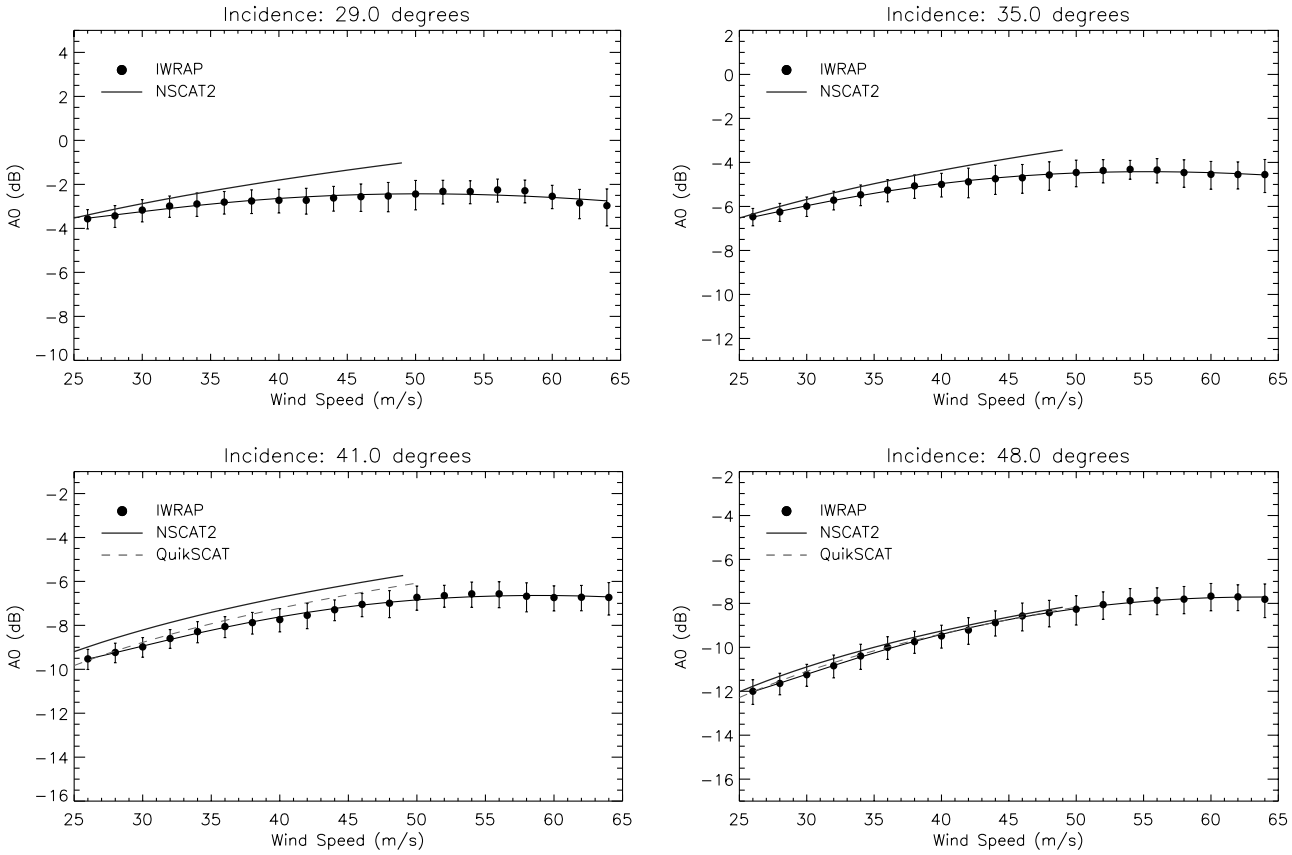

Figure 8. Averaged IWRAP A_0 measurements at Ku-band and H polarization (solid circles) plotted versus the mean U_{10N} estimates. The error bars show the standard deviations of the A_0 measurements within each 2 m s^{-1} wind speed bin. From these measurements, the derived high wind speed IWRAP GMF (discussed in section 4) is also plotted (solid black line). The NSCAT2 (dash-dot-dotted line) and QuikSCAT (dashed line) GMFs are overlaid. The QuikSCAT GMF is only available for incidences ranging from 40 to 50 degrees.

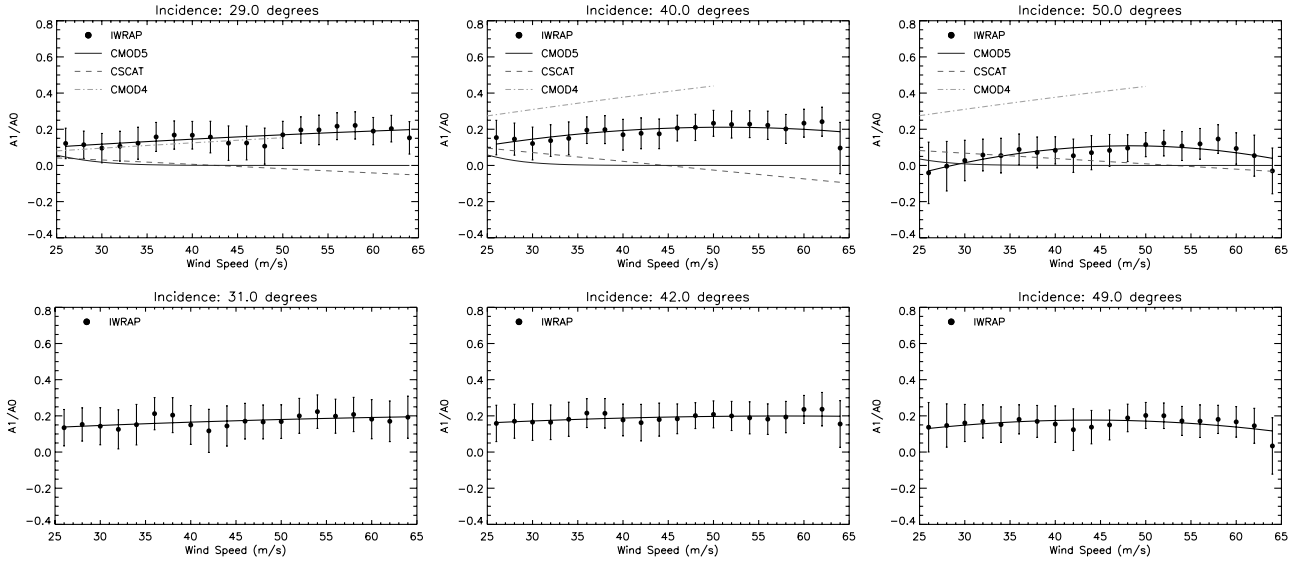

Figure 9. Averaged IWRAP A_1 measurements (solid circles) at C-band for V (top) and H (bottom) polarizations plotted versus the mean U_{10N} estimates at roughly 30, 40, and 50 degrees incidence. Standard deviations of the A_1 measurements within each 2 m s^{-1} wind speed bin are shown by the vertical lines. From these measurements, the derived high wind speed IWRAP GMF (discussed in section 4) is also plotted (solid black line). The CMOD-5 (dash-dotted line) and CSCAT (dashed line) GMFs are overlaid at V polarization. There is currently no other GMF for this frequency band at H polarization.

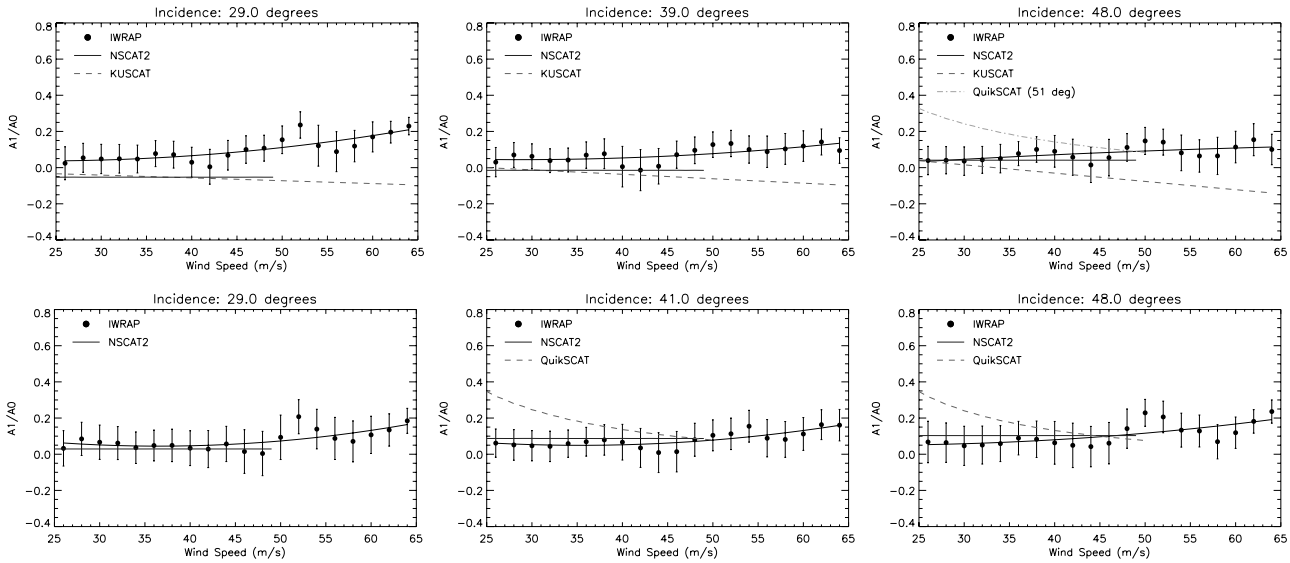

Figure 10. Averaged IWRAP A_1 measurements (solid circles) at Ku-band for (top) V and (bottom) H polarizations plotted versus the mean U_{10N} estimates at roughly 30, 40, and 50 degrees incidence. Standard deviations of the A_1 measurements within each 2 m s^{-1} wind speed bin are shown by the vertical lines. From these measurements, the derived high wind speed IWRAP GMF (discussed in section 4) is also plotted (solid black line). At V polarization, the NSCAT2 (dash-dot-dotted line), KUSCAT (dashed line), and QuikSCAT GMF (dash-dotted line) GMFs are overlaid. The QuikSCAT GMF is shown at 51 degrees incidence since it is only available for incidence angles ranging from 51 to 60 degrees. At H polarization, the NSCAT2 (dash-dot-dotted line) and QuikSCAT (dashed line) GMFs are overlaid. At this polarization, the QuikSCAT GMF is only available for incidences ranging from 40 to 50 degrees.

obvious than in the rest of the cases, especially at Ku-band where the A_0 starts decreasing rapidly after $U_{10N_{sat}}$ is reached.

[34] To model the departure from a power law, it is enough to add one more term at C-band, resulting in a parabolic fitting in a space where both the wind speed and the A_0 are in logarithmic scale, hereafter referred to as log-log space. At Ku-band, the fast decrease in the A_0 measurements at the highest wind speeds requires a higher-order polynomial, and so a cubic fitting in log-log space has been used. The functional form for the C-Band high wind speed GMF A_0 is thus given by

$$A_{0_{dB}}(U_{10N}) = 10 \cdot \left[\beta + \gamma_1 \cdot \log_{10}(U_{10N}) + \gamma_2 \cdot [\log_{10}(U_{10N})]^2\right], \tag{10}$$

where A_0 is in dB. In linear space this translates to

$$A_0(U_{10N}) = [10]^{\beta} \cdot [U_{10N}]^{\gamma_1} \cdot [U_{10N}]^{\gamma_2 \cdot \log_{10}(U_{10N})}. \tag{11}$$

At Ku-band, the functional form for the high wind speeds GMF A_0 is given by

$$A_{0_{dB}}(U_{10N}) = 10 \cdot \left[\beta + \gamma_1 \cdot \log_{10}(U_{10N}) + \gamma_2 \cdot [\log_{10}(U_{10N})]^2 + \gamma_3 \cdot [\log_{10}(U_{10N})]^3\right], \tag{12}$$

where A_0 is in dB. The coefficients in equations (6) through (8) are determined using a linear regression, and Table 2 lists the values for the coefficients. The new high wind speed GMF A_0 values are plotted as a solid line in Figures 5 through 8.

[35] Given equation (3), $U_{10N_{sat}}$ can be derived by evaluating the first derivative. For C-band, it is given by the expression

$$U_{10N_{sat}} = [10]^{-\frac{\gamma_1}{2\gamma_2}}. \tag{13}$$

At Ku-band, the expression has two solutions, and therefore the saturation speed needs to be determined manually,

$$U_{10N_{sat}} = [10]^{\frac{-2\gamma_2 \pm \sqrt{4\gamma_2^2 - 12\gamma_1\gamma_3}}{2\gamma_1}}. \tag{14}$$

[36] Table 3 lists $U_{10N_{sat}}$ values for C- and Ku-band and for each incidence angle. The Ku-band $U_{10N_{sat}}$ values increase with incidence angle. This is consistent with the concept that the capillary-gravity wave number spectra is saturating. The $U_{10N_{sat}}$ values at C-band and V polarization follow this trend as well. However, the observed saturation values are closer to the 65 m s^{-1} maximum observed wind speed, and therefore the maximum is not as well defined as in the Ku-band observations where it occurs at a much lower wind speed. At H polarization, the fit predicts saturation wind speeds above the maximum observed wind speed except at 31.0 degrees incidence. This is consistent with the A_0 plots, which suggest that the saturation point may happen at even higher wind speeds. It is worth noting that this does not imply that the backscatter response still

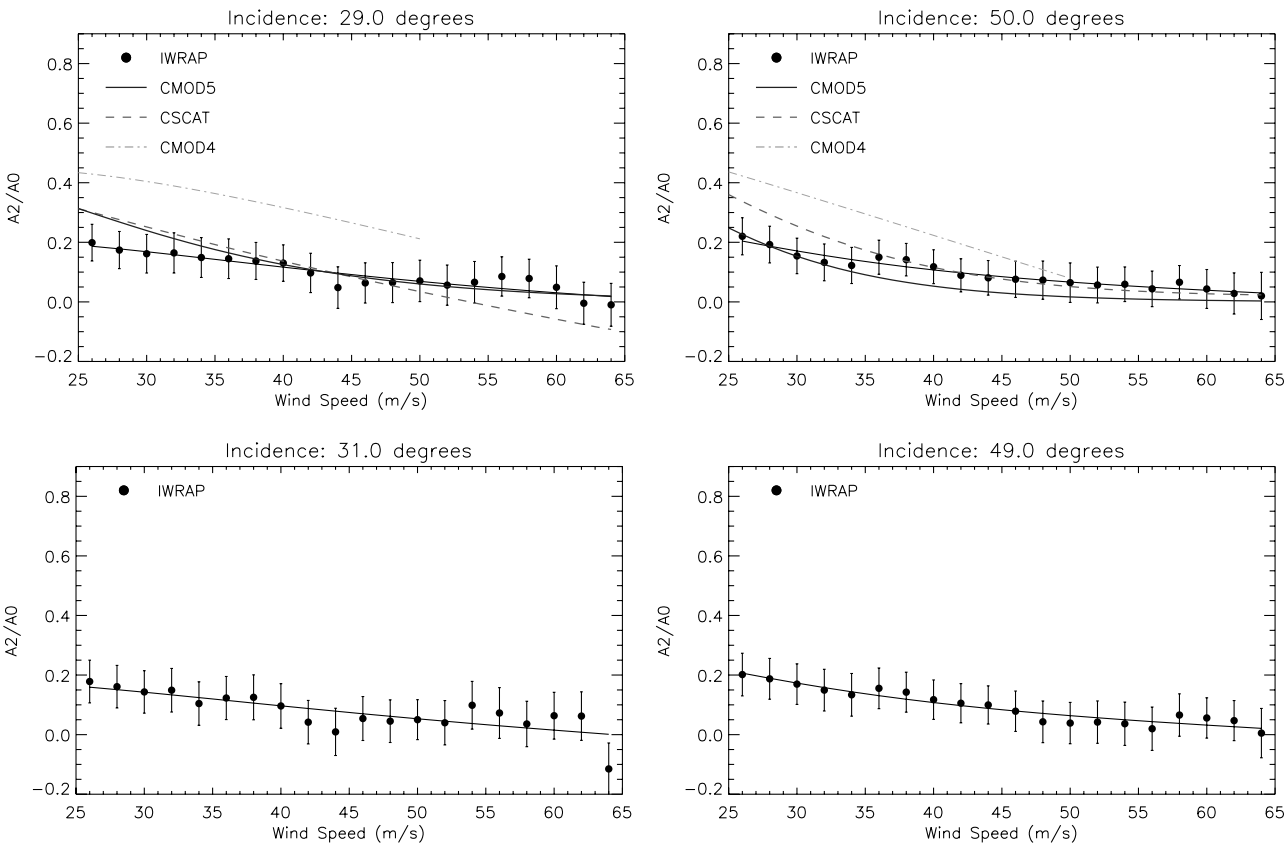

Figure 11. Averaged IWRAP A_2 measurements (solid circles) at C-band and (top) V and (bottom) H polarizations are plotted versus the mean U_{10N} estimates. Standard deviations of the A_2 measurements within each 2 m s^{-1} wind speed bin are shown by the vertical lines. From these measurements, the derived high wind speed IWRAP GMF (discussed in section 4) is also plotted (solid black line). At V polarization, the CMOD-5 (dash-dotted line) and CSCAT (dashed line) GMFs are overlaid. At V-polarization, there is currently no other GMF for this frequency band.

follows a power law and that no saturation is present; the response is saturated with respect to a power law, but the saturation happens to be much slower; that is, the departure from a power law response is not as strong as at V polarization, and the A_0 response does not hint a decreasing trend within the measured range of wind speeds. To make this clear, Figure 13 shows the fitted A_0 models, normalized in linear space with respect to the mean NRCS at 25 m s^{-1}, i.e., $A_0/A_0(U_{10N} = 25$ m s$^{-1})$, for both frequency bands, both polarizations and all incidence angles, versus the wind speed in log scale. If the A_0 response follows a power law, in log-log space it should appear as a straight line. However, we can see how this is not true for any of the cases, and the departure from a power law happens sooner for smaller incidence angles, as already discussed.

[37] The high wind speed GMF must also include the wind directional signature in the NRCS. The functional form for the full high wind speed GMF is modeled using a form similar to the CMOD4, CSCAT and KUSCAT models, given by the expression

$$\sigma^\circ(\theta, U_{10N}, \chi) = A_0(\theta, U_{10N})[1 + a_1(\theta, U_{10N})\cos(\chi_{rel}) \quad (15)$$

$$+a_2(\theta, U_{10N})\cos(2\chi_{rel})], \quad (16)$$

where $\chi_{rel} = \chi_{up} - \chi$ and

$$a_1(\theta, U_{10N}) = c_0(\theta, U_{10N}) + c_1(\theta, U_{10N})U_{10N} \quad (17)$$

$$+c_2(\theta, U_{10N})U_{10N}^2, \quad (18)$$

$$a_2(\theta, U_{10N}) = d_0(\theta, U_{10N}) + d_1(\theta, U_{10N})U_{10N} + d_2(\theta, U_{10N})\tanh \cdot \left(\frac{U_{10N}}{d_3(\theta)}\right)U_{10N}, \quad (19)$$

and σ° is the NRCS. The first harmonic is thus modeled by a second-order polynomial and the second harmonic by a linear relationship plus a hyperbolic tangent to capture the saturation at high wind speeds. Setting the d_3 values to those of *Donnelly et al.* [1999], the other coefficients can be derived using a linear regression. For more discussion on coefficient d_3, the reader is referred to *Donnelly et al.* [1999]. Tables 4 and 5 list the fit coefficients. The predicted a_1 and a_2 values using the above fits are plotted in Figures 9 through 12 as solid lines.

[38] The new GMFs presented in this paper correspond to the particular incidence angles at which the radar instrument operates (roughly 30, 35, 40 and 50 degrees incidence). It is

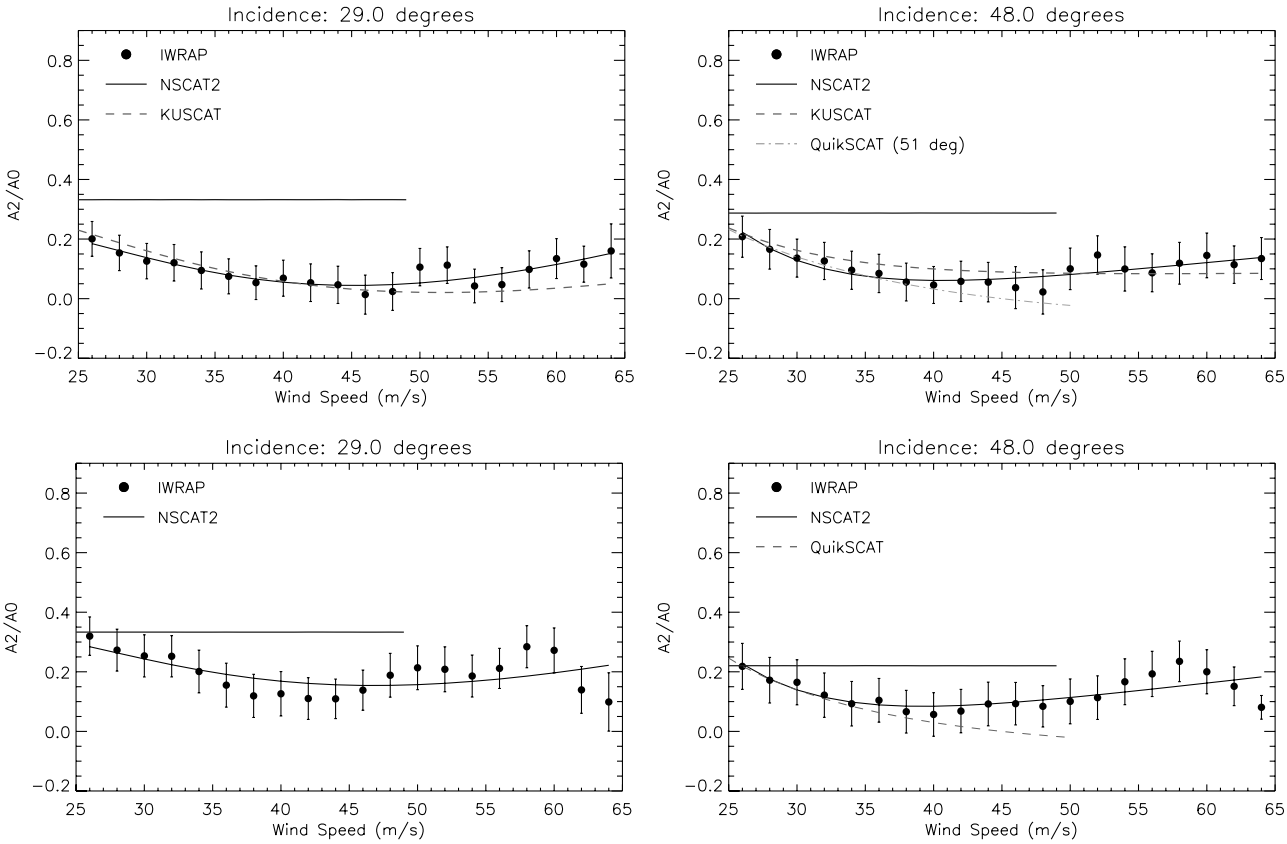

Figure 12. Averaged IWRAP A_2 measurements (solid circles) at Ku-band and (top) V and (bottom) H polarizations are plotted versus the mean U_{10N} estimates. Standard deviations of the A_2 measurements within each 2 m s^{-1} wind speed bin are shown by the vertical lines. From these measurements, the derived high wind speed IWRAP GMF (discussed in section 4) is also plotted (solid black line). At V polarization, the NSCAT2 (dash-dot-dotted line), KUSCAT (dashed line), and QuikSCAT (dash-dotted line) GMFs are overlaid. The V-polarized QuikSCAT GMF is shown at 51 degrees incidence since it is only available for incidences ranging from 51 to 60 degrees. At H polarization the NSCAT2 (dash-dot-dotted line) and QuikSCAT (dashed line) GMFs are overlaid. The H-polarized QuikSCAT GMF is only available for incidences ranging from 40 to 50 degrees.

important to note that it is possible to interpolate the models offered here anywhere within the range of these observations in order to derive models at different incidence angles of particular interest. Given the wide range of possibilities in terms of interpolation techniques, the choice of the technique is best left to the reader. On the other hand, interpolation in frequency (e.g., as to derive a GMF at X-Band) may not yield entirely satisfactory results given the fact that the physics behind the backscattering processes are different at different wavelengths. However, this could be improved if measurements at least within the frequency bands where there are fundamental changes in the physical processes involved are incorporated into the interpolation process.

5. Conclusions

[39] Airborne C- and Ku-band ocean surface NRCS measurements, obtained with the IWRAP instrument in surface wind conditions from 25 to 65 m s^{-1}, were presented. These measurements clearly show that the ocean surface NRCS saturates at hurricane force winds. It has also been shown how the mean NRCS response clearly departs from a power law for all frequency bands, polarizations and incidence angles. The observed saturation wind speed depends on the electromagnetic wavelength, polarization

Table 2. New High Wind Speed GMF: A_0 Coefficients

Band	Polarization	Incidence, degrees	β	γ_1	γ_2	γ_3
C	V	29.0	−3.807	4.064	−1.185	
C	V	34.0	−4.631	4.641	−1.300	
C	V	40.0	−5.081	4.784	−1.266	
C	V	50.0	−6.931	6.808	−1.903	
C	H	31.0	−4.892	4.7275	−1.3598	
C	H	36.0	−5.689	5.2932	−1.4401	
C	H	42.0	−5.570	4.6925	−1.1496	
C	H	49.0	−5.886	4.5876	−1.0355	
Ku	V	29.0	56.624	−110.1	70.504	−14.95
Ku	V	34.0	22.714	−47.25	31.540	−6.905
Ku	V	39.0	30.943	−64.01	42.585	−9.304
Ku	V	48.0	6.344	−17.90	13.439	−3.162
Ku	H	29.0	12.602	−26.929	18.342	−4.086
Ku	H	35.0	12.640	−28.401	19.673	−4.409
Ku	H	41.0	17.347	−38.006	25.731	−5.646
Ku	H	48.0	23.317	−50.369	33.627	−7.269

Table 3. Saturation Wind Speeds

Band	Polarization	Incidence, degrees	$U_{10N_{sat}}$, m s^{-1}
C	V	29.0	51.9
C	V	34.0	60.9
C	V	40.0	61.0
C	V	50.0	61.5
C	H	31.0	54.7
C	H	36.0	>65
C	H	42.0	>65
C	H	49.0	>65
Ku	V	29.0	50.5
Ku	V	34.0	51.8
Ku	V	39.0	51.4
Ku	V	48.0	57.9
Ku	H	29.0	50.3
Ku	H	35.5	55.2
Ku	H	41.0	58.8
Ku	H	48.0	63.5

and incidence angle. Besides the saturation in the wind speed suggested by the A_0 measurements, there is an equivalent saturation in the wind direction which is manifested through the small values indicated by first and second harmonics.

[40] The observations also show a higher sensitivity with the wind speed at H polarization for both frequency bands than at V polarization. On the other hand, at Ku-band and V polarization, the mean NRCS starts decreasing more rapidly than any of the other frequency bands or polarization. This can therefore result in a more complex scenario for wind vector retrieval algorithms due to the ambiguity of the NRCS values after certain wind speed.

[41] The saturation in the azimuthal response of the NRCS is also very apparent in all cases, resulting in an overall flattening of the response around the downwind direction. This introduces serious limitations in the attainable accuracy of the wind direction at the highest wind speeds. In most cases, however, the signature reappears above 50 to 55 m s^{-1}. On the other hand, the upwind signature is always present.

[42] The CMOD4, CMOD5, NSCAT2 and QuikSCAT GMFs do not capture this saturation, nor do they adequately predict the reduced NRCS sensitivity to the wind speed and direction prior to the saturation. Thus these models overpredict the NRCS for wind speeds over 35 m s^{-1}. New C- and Ku-band high wind speed GMFs, developed in

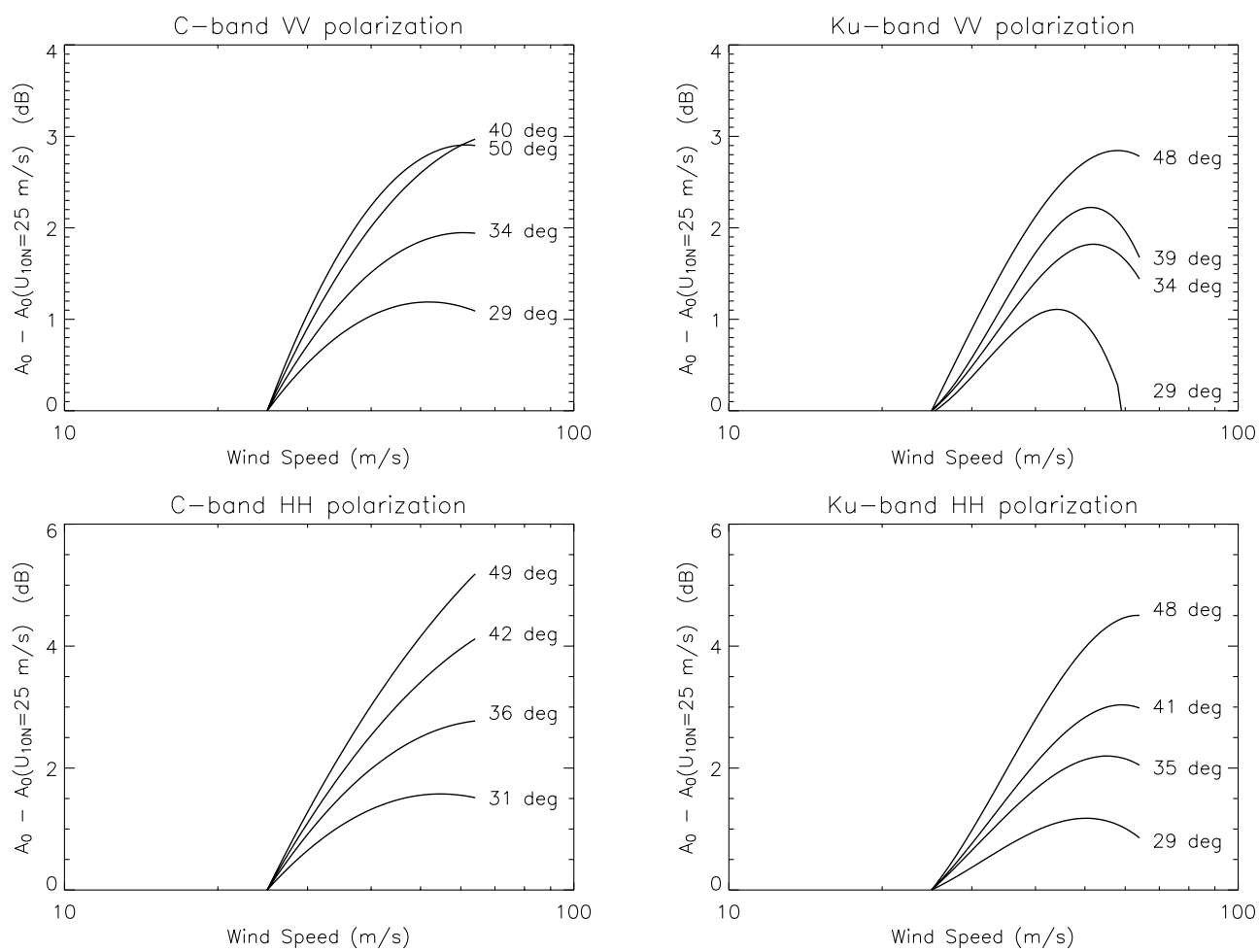

Figure 13. Fitted A_0 models for all frequency bands, polarizations, and incidence angles versus the wind speed in log scale. For each case, the particular A_0 offset at 25 m s^{-1} has been removed to normalize all the curves to a common starting point. This figure clearly illustrates the saturating behavior of the mean NRCS for all cases, as well as the deviation from a power law model (manifested as a departure from a straight line).

Table 4. New High Wind Speed GMF: A_1 Coefficients

Band	Polarization	Incidence, degrees	c_0	c_1	c_2
C	V	29.0	1.500×10^{-2}	3.917×10^{-3}	-1.6595×10^{-5}
C	V	34.0	-1.080×10^{-2}	7.046×10^{-3}	-4.6334×10^{-5}
C	V	40.0	-1.757×10^{-1}	1.515×10^{-2}	-14.830×10^{-5}
C	V	50.0	-5.453×10^{-1}	2.710×10^{-2}	-28.064×10^{-5}
C	H	31.0	7.030×10^{-2}	3.093×10^{-3}	-1.8011×10^{-5}
C	H	36.0	-1.083×10^{-1}	1.354×10^{-2}	-13.004×10^{-5}
C	H	42.0	8.060×10^{-2}	4.091×10^{-3}	-3.5243×10^{-5}
C	H	49.0	-1.053×10^{-1}	1.289×10^{-2}	-14.723×10^{-5}
Ku	V	29.0	9.332×10^{-2}	-4.844×10^{-3}	10.399×10^{-5}
Ku	V	34.0	3.097×10^{-1}	-1.482×10^{-2}	20.363×10^{-5}
Ku	V	39.0	1.028×10^{-1}	-4.123×10^{-3}	7.221×10^{-5}
Ku	V	48.0	-5.388×10^{-2}	3.959×10^{-3}	-2.092×10^{-5}
Ku	H	29.0	2.556×10^{-1}	-1.156×10^{-2}	15.821×10^{-5}
Ku	H	35.0	3.349×10^{-1}	-1.454×10^{-2}	19.262×10^{-5}
Ku	H	41.0	2.177×10^{-1}	-9.540×10^{-3}	13.495×10^{-5}
Ku	H	48.0	7.829×10^{-2}	-2.835×10^{-3}	7.192×10^{-5}

section 4, model the saturation in the NRCS. These results are in good agreement at the lower wind speeds with the CSCAT and KUSCAT GMFs developed from measurements acquired with the UMass C- and Ku-band scatterometers. Note that both these instruments, as well as the data sets from which the corresponding GMFs were derived, are totally different from the IWRAP instrument and the data sets used in this paper, therefore constituting a totally independent source for comparisons. Disagreements at the higher wind speeds are attributed to the presence of rain contaminated measurements in the derivation of the CSCAT and KUSCAT GMFs. While the scatterometers sampled only the ocean backscatter, IWRAP provides collocated measurements of the volume backscatter from rain from the aircraft down to the ocean surface every 30 m together with every NRCS measurement. The presence of rain can therefore be checked, and the rain flagged measurements have been removed for this analysis.

[43] As a result of these observations, complex scenarios can arise when retrieving hurricane-force winds from the measurements owing to the reduced sensitivity or saturation in the NRCS. C-band measurements, particularly at H polarization and high incidence angles, seem more suitable given that the saturation in the NRCS occurs at a higher wind speed than at Ku-band. In fact, the saturation in the wind speed is not reached even at wind speeds as high as 65 m s^{-1} and the departure of the A_0 response from a power law is not as significant as in the rest of the cases. On the other hand, the wind direction shows clear signs of saturation, thereby imposing difficulties in the retrieval of ocean surface wind directions at very high wind speeds.

[44] However, both C- and Ku-band satellite-based scatterometers are capable of measuring the hurricane-force wind radii thanks to the large scale of these systems. Improving the spatial resolution of the satellite-based scatterometer measurements will not necessarily result in higher wind speeds being retrieved owing to the saturation effect. In fact, the retrieved wind speeds will actually show a larger difference when compared to the true wind speed for smaller spatial scales. Again, high incidence angles at C-band and H polarization seem to be the best option for future high-resolution satellite-based scatterometers, since at least the saturation in the wind speed is not as significant. Moreover, it should be noted that higher-resolution measurements will aid in seeing through precipitation events that often occur on the scales of a couple of kilometers, as well as reduce biases introduced by sampling over wind speed gradients.

Table 5. New High Wind Speed GMF: A_2 Coefficients

Band	Polarization	Incidence, degrees	d_0	d_1	d_2	d_3
C	V	29.0	6.021×10^{-2}	1.904×10^{-2}	-2.026×10^{-2}	30.0
C	V	34.0	-4.288×10^{-2}	6.199×10^{-2}	-6.066×10^{-2}	20.0
C	V	40.0	1.972×10^{-1}	2.561×10^{-2}	-2.837×10^{-2}	18.0
C	V	50.0	1.291×10^{-1}	3.551×10^{-2}	-3.714×10^{-2}	19.0
C	H	31.0	1.337×10^{-1}	8.883×10^{-3}	-1.121×10^{-2}	30.0
C	H	36.0	-2.461×10^{-1}	8.731×10^{-2}	-8.289×10^{-2}	20.0
C	H	42.0	2.864×10^{-1}	-1.006×10^{-3}	-3.737×10^{-3}	18.0
C	H	49.0	1.534×10^{-1}	3.223×10^{-2}	-3.438×10^{-2}	19.0
Ku	V	29.0	-8.451×10^{-1}	1.472×10^{-1}	-1.326×10^{-1}	23.0
Ku	V	34.0	-8.396×10^{-1}	2.065×10^{-1}	-1.895×10^{-1}	20.0
Ku	V	39.0	-1.941×10^{-1}	4.710×10^{-1}	-4.658×10^{-1}	12.0
Ku	V	48.0	1.496×10^{-1}	5.652×10^{-1}	-5.608×10^{-1}	11.0
Ku	H	29.0	-5.048×10^{-1}	1.153×10^{-1}	-1.048×10^{-1}	23.0
Ku	H	35.0	-6.197×10^{-1}	1.489×10^{-1}	-1.355×10^{-1}	20.0
Ku	H	41.0	-7.876×10^{-2}	3.780×10^{-1}	-3.742×10^{-1}	12.0
Ku	H	48.0	-1.586×10^{-1}	5.455×10^{-1}	-5.401×10^{-1}	11.0

[45] The new GMFs presented in this paper should be incorporated into current retrieval algorithms. Their improved characterization of the NRCS dependence on wind speed and direction will result in better retrieved wind fields using satellite-based scatterometers. Finally, more information and measurements of the ocean surface drag coefficient are needed to better understand why the NRCS is saturating. This paper suggests that the capillary-gravity wave spectra saturates in hurricane-force conditions, and that the decrease in the NRCS at the very high wind speeds might be caused by a decoupling of the surface winds and the ocean surface which results in reduced small-scale roughness. In that scenario, after a certain saturation wind speed is reached, the transfer of momentum from the wind forcing into the ocean surface stops increasing with an increasing wind speed, and actually decreases as if the real wind forcing applied was due to a smaller wind speed.

[46] **Acknowledgments.** The authors wish to thank Beth Kerr from UMass for her support during the 2003 hurricane season, as well as J. McFadden, J. Barr, and S. McMillan, along with the technicians, flight engineers, machinists, pilots, and crew of NOAA N42RF for their countless hours of support. This investigation was funded by NASA/JPL grant 1217185, JPL grant 1201304, USWRP/NASA grant NAG8-1490, NOAA/NESDIS Ocean Remote Sensing Program (contract 40-AA-NE-00598), NOAA/NESDIS grant NA17EC1348, and ONR (Remote Sensing) grant N00014-01-1-0923.

References

Carswell, J. R., S. C. Carson, R. E. McIntosh, F. K. Li, G. Neumann, D. McLaughlin, J. C. Wilkerson, P. G. Black, and S. V. Nghiem (1994), Airborne scatterometers: Investigating ocean backscatter under low- and high-wind conditions, *Proc. IEEE*, *82*(12), 1835–1860.

Carswell, J., E. J. Knapp, P. S. Chang, P. D. Black, and F. D. Marks (2000), Limitations of scatterometry high wind speed retrieval, paper presented at International Geoscience and Remote Sensing Symposium, Inst. of Electr. and Electron. Eng., New York.

Donelan, M., and W. Pierson (1987), Radar scattering and equilibrium ranges in wind-generated waves with application to scatterometry, *J. Geophys. Res.*, *92*(C5), 4971–5029.

Donelan, M. A., B. K. Haus, N. Reul, W. J. Plant, M. Stiassne, H. C. Graber, O. B. Brown, and E. S. Saltzman (2004), On the limiting aerodynamic roughness of the ocean in very strong winds, *Geophys. Res. Lett.*, *31*, L18306, doi:10.1029/2004GL019460.

Donnelly, W., J. Carswell, R. McIntosh, P. S. Chang, J. Wilkerson, P. Black, and F. Marks (1999), Revised ocean backscatter models at c and ku-band under high wind conditions, *J. Geophy. Res.*, *104*(C5), 11,485–11,497.

Doviak, R. J., and D. S. Zrnic (1984), *Doppler Radar and Weather Observations*, 2nd ed., Elsevier, New York.

Fernandez, D. E., E. Kerr, A. Castells, S. Frasier, J. Carswell, P. S. Chang, P. Black, and F. Marks (2005), IWRAP: The Imaging Wind and Rain Airborne Profiler for remote sensing of the ocean and the atmospheric boundary layer within tropical cyclones, *IEEE Trans. Geosci. Remote Sens.*, *43*(8), doi:10.1109/TGRS.2005.851640.

Hersbach, H. (2003), An improved geophysical model function for ERS C-band scatterometry, *Tech. Memo 395*, Eur. Cent. for Medium-Range Weather Forecast., Reading, U. K.

Isaksen, L., and A. Stoffelen (2000), ERS scatterometer wind data impact on ECMWF's tropical cyclone forecasts, *IEEE Trans. Geosci. Remote Sens.*, *38*(4), doi:10.1109/36.851771.

Jones, W. L., P. Black, V. Delnore, and C. Swift (1981), Airborne microwave remote sensing measurement of Hurricane Allen, *Science*, *214*, 274–280.

Jones, W., V. Cardone, W. Pierson, J. Zec, L. Rice, A. Cox, and W. Sylvester (1999), NSCAT high-resolution surface wind measurements in typhoon violet, *J. Geophys. Res.*, *104*(C5), 11,247–11,260.

Katsaros, K., E. Forde, P. Chang, and W. Liu (2000), QuikSCAT facilitates early identification of tropical depressions in 1999 hurricane season, *Geophys. Res. Lett.*, *28*(6), 1043–1046.

Knapp, E., J. Carswell, and C. Swift (2000), A dual polarization multi-frequency microwave radiometer, paper presented at International Geoscience and Remote Sensing Symposium, Inst. of Electr. and Electron. Eng., New York.

Marks, F., and L. Shay (1998), Landfalling tropical cyclones: Forecast problems and associated research opportunities: Report of the fifth prospectus Development team to the U.S. Weather Research Program, *Bull. Am. Meteorol. Soc.*, *79*, 305–323.

McAdie, C., and M. Lawrence (1993), Long-term trends in National Hurricane Center track forecast errors in the Atlantic basin, paper presented at Conference on Hurricanes and Tropical Meteorology, Am. Meteorol. Soc., Miami, Fla.

Plant, W. J. (1986), A two-scale model of short wind-generated waves and scatterometry, *J. Geophys. Res.*, *91*(C9), 735–749.

Powell, M. D., P. J. Vickery, and T. A. Reinhold (2003), Reduced drag coefficient for high wind speeds in tropical cyclones, *Nature*, *422*(6929), doi:10.1038/nature01481.

Quilfen, Y., B. Chapron, T. Elfouhaily, K. Katsaros, and J. Tournadre (1998), Observation of tropical cyclones by high-resolution scatterometry, *J. Geophys. Res.*, *103*(C4), 7767–7786.

Sheets, R. C. (1990), The National Hurricane Center—Past, present, and future, *Weather Forecast.*, *5*(2), doi:10.1175/1520-0434.

Stoffelen, A., and D. Anderson (1997), Scatterometer data interpretation: Estimation and validation of the transfer function CMOD4, *J. Geophys. Res.*, *102*(C3), 5767–5780.

Uhlhorn, E. W., and P. G. Black (2003), Verification of remotely sensed sea surface winds in hurricanes, *J. Atmos. Oceanic Technol.*, *20*(1), doi:10.1175/1520-0426.

Wentz, F., and D. Smith (1999), A model function for the ocean-normalized radar cross section at 14 GHz derived from NSCAT1, *J. Geophys. Res.*, *104*(C5), 11,499–11,514.

Yueh, S., R. West, F. Li, W. Tsai, and R. Lay (2000), Dual-polarized ku-band backscatter signatures of hurricane ocean winds, *IEEE Trans. Geosci. Remote Sens.*, *38*(1), doi:10.1175/1520-0426.

Yueh, S. H., B. W. Stiles, W. Y. Tsai, H. Hu, and W. T. Liu (2001), QuikSCAT geophysical model function for tropical cyclones and application to Hurricane Floyd, *IEEE Trans. Geosci. and Remote Sens.*, *39*(12), 2601–2612.

Yueh, S. H., B. W. Stiles, and W. T. Liu (2003), QuikSCAT wind retrievals for tropical cyclones, *IEEE Trans.Geosci. and Remote Sens.*, *41*(11), doi:10.1109/TGRS.2003.814913.

P. G. Black and F. M. Marks, Hurricane Research Division, NOAA/AOML, 4301 Rickenbacker Causeway, Miami, FL 33149, USA. (peter.black@noaa.gov; frank.marks@noaa.gov)

J. R. Carswell, Remote Sensing Solutions, Barnstable, MA 02630, USA. (carswell@rmss.us)

P. S. Chang and D. E. Fernandez, NOAA/NESDIS/ORA, World Weather Building, Room 102A, 5200 Auth Road, Camp Springs, MD 20746, USA. (paul.s.chang@noaa.gov; daniel.fernandez@noaa.gov)

S. Frasier, University of Massachusetts, Knowles Engineering Building, Amherst, MA 01003, USA. (frasier@ecs.umass.edu)